

pubs.acs.org/JACS Article

Tailoring Lewis Acidity of Metal Oxides on Nickel to Boost Electrocatalytic Hydrogen Evolution in Neutral Electrolyte

Lin-Lin Wang, Xiao-Ran Wang, Hong-Juan Wang, Chong Zhang, Jing-Jing Li, Guo-Jin Feng, Xuan-Xuan Cheng, Xue-Rong Qin, Zi-You Yu, and Tong-Bu Lu*



Cite This: J. Am. Chem. Soc. 2025, 147, 7555-7563

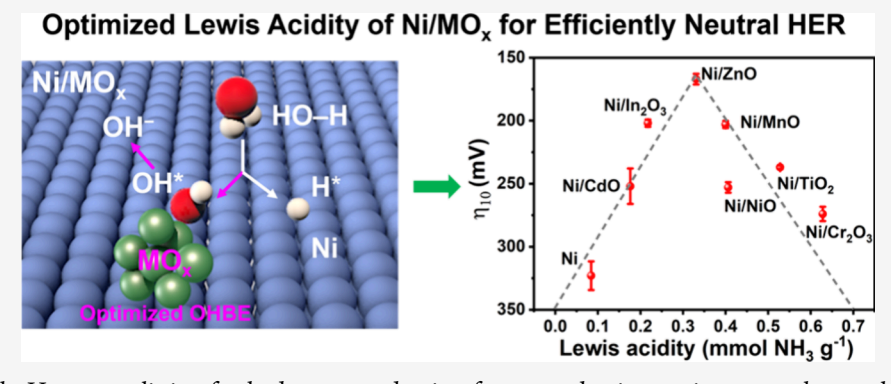


ACCESS I

III Metrics & More

Article Recommendations

s Supporting Information



ABSTRACT: Neutral-pH water splitting for hydrogen production features a benign environment that could alleviate catalyst and electrolyzer corrosion but calls for the corresponding high-efficiency and earth-abundant hydrogen evolution reaction (HER) catalysts. Herein, we first designed a series of metal oxides decorated on Ni as the model catalysts and found a volcano-shaped relationship between the Lewis acidity of Ni/metal oxides and HER activity in neutral media. The Ni/ZnO with the optimum Lewis acidity could balance water dissociation and hydroxyl desorption, thereby greatly boosting the HER. On the basis of this finding, we further in situ grew the Ni/ZnO heterostructure on a three-dimensional conductive support. The resulting catalyst requires overpotentials of merely 34 and 194 mV to deliver the current densities of 10 and 200 mA cm⁻², respectively, and can stably operate at these current densities for 2000 h in 1 M phosphate buffer solution (pH 7), representing the most active and durable HER catalyst in neutral electrolyte reported thus far. Our work provides an effective design scheme for low-cost and high-performance neutral HER catalysts.

■ INTRODUCTION

Hydrogen, as a vital chemical feedstock and an energy carrier, has been widely used in many industrial fields, including petroleum refining, ammonia production, and fuel cell vehicles.¹⁻³ Compared with hydrogen production from fossil fuels, water electrolysis powered by renewable electricity can provide great promise to produce clean hydrogen with an emission-free route.⁴⁻⁶ The electrocatalytic hydrogen evolution reaction (HER) can be performed in either acidic, neutral, or alkaline media.⁷⁻⁹ The HER operating in a mildly neutral environment has attracted much attention, as it could extend the catalyst option, alleviate the catalyst and electrolyzer corrosion, and offer the potential feasibility for the direct seawater electrolysis. 10-15 Although Pt-based materials have been well-known as the benchmark catalysts for HER, their high cost limits the large-scale application. 5,16,17 Therefore, it is highly required to design and develop nonprecious HER catalysts with high performance for the low-cost neutral water splitting.

Previous studies revealed that alkaline/neutral HER begins with the Volmer step ($H_2O + e^- \rightarrow H^* + OH^-$) and is followed by the Heyrovsky or Tafel step (hydrogen combination step). Essentially, the Volmer step involves the initial water dissociation step ($H_2O \rightarrow H^* + OH^*$) and the subsequent OH* desorption step (OH* + $e^- \rightarrow OH^-$). Among these earth-abundant HER catalysts, Ni-based materials with high conductivity and cheap price have been investigated for alkaline/neutral HER catalysis. However, metallic Ni usually exhibits the unsatisfactory HER activity, probably owing to the poor water dissociation ability. Probably owing to the poor water dissociation ability.

Received: November 22, 2024
Revised: January 20, 2025
Accepted: February 5, 2025
Published: February 18, 2025





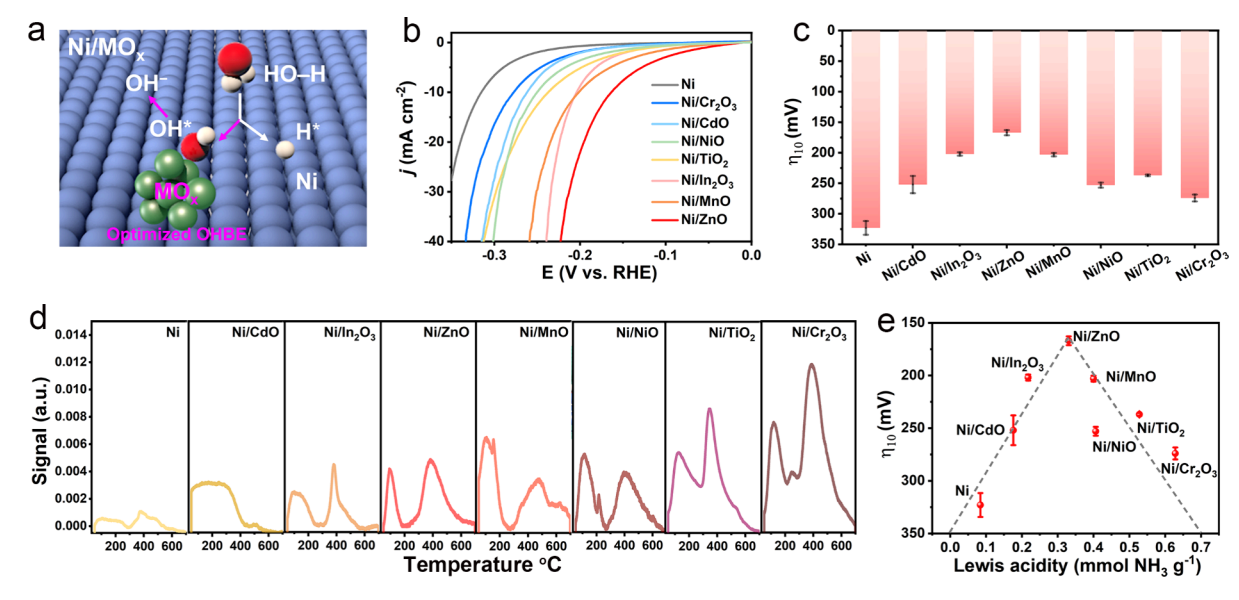


Figure 1. HER performance for Ni/MO $_x$ catalysts in neutral electrolyte. (a) Schematic illustration of the accelerated Volmer step for HER through a designed Ni/MO $_x$ heterostructure catalyst. (b) HER polarization curves with the iR correction for Ni and Ni/MO $_x$ catalysts in 1 M PBS. (c) The overpotentials at 10 mA cm $^{-2}$ for Ni and Ni/MO $_x$ catalysts. (d) NH $_3$ -TPD curves for Ni and Ni/MO $_x$ catalysts. (e) Correlation between the HER activity and Lewis acidity for Ni and Ni/MO $_x$ catalysts, showing a volcano-like relationship. The error bars represent the standard deviation of three independent HER activity measurements.

strategy is introducing the oxophilic component, where the oxophilic site binds with OH* and the Ni site binds with H* to cleave the H–OH bonds of H₂O molecule for the facilitated water dissociation. ^{25,26,28} Various transition-metal oxides and hydroxides have been reported as the oxophilic components to couple with Ni for the formation of the heterostructure catalysts, such as Ni/NiO, ^{26,29} Ni/Ln₂O₃, ²⁵ Ni/V₂O₃, ^{30,31} Ni/Mn₃O₄, ³² Ni/NiO/MoO₃, ³³ Ni/Ni(OH)₂, ^{34–36} Ni/NiFe-(OH)_x, ³⁷ and so on. Although these heterostructure catalysts could efficiently boost the alkaline HER, the HER performance in neutral media has rarely been explored. In addition, according to the Brønsted–Evans–Polanyi principle, the toostrong OH* adsorption on the oxophilic species would inhibit OH* desorption in the Volmer step, resulting in the accumulation of OH* on the active sites to impede the water readsorption. ^{20,25,38} In this regard, how the various oxophilic species affect the HER activity of Ni and whether the option of oxophilic species is proper have never been fully elucidated

Recently, to investigate the effect of adsorbed OH* on the HER activity of Pt in alkaline media, Koper et al. used the Pt(553) single-crystal electrode as a model surface and deposited various metal atoms with variable OH* binding energy (OHBE) at the Pt step edge.²⁰ This specific structure is sufficiently simple to construct the model and calculate the OHBE using density functional theory (DFT). Their alkaline HER activities exhibited a volcano-shape relationship with the DFT-calculated OHBE, indicating that an optimum OHBE is required. 20,25 Nevertheless, the structures of Ni-based heterostructure catalysts are not well-defined, and the accurate determination of the OHBE from DFT is relatively timeconsuming. 20,39 Therefore, it is urgent to experimentally seek a suitable activity descriptor and correlate the measured activity descriptor with HER activity, thereby guiding the achievement of high-performance Ni-based HER catalysts in neutral media.

Herein, we first constructed various metal oxides decorated on Ni (denoted as Ni/ MO_{xy} M = Ti, Cr, Mn, Ni, Zn, Cd, or

In) as the model catalysts and found that the HER activities of Ni/MO $_x$ catalysts exhibit a volcano-like trend as a function of the Lewis acidity of catalysts in a neutral electrolyte. As the Lewis acidity can well-reflect the OH* binding ability, Ni/ZnO with the proper Lewis acidity can greatly boost the Volmer step by optimizing the water dissociation as well as the OH* desorption. Further, the Ni/ZnO heterostructure was in situ grown on the three-dimensional conductive substrate (denoted as 3D-Ni/ZnO) to expose more active sites. The obtained catalyst requires small overpotentials of 34 and 194 mV to achieve 10 and 200 mA cm $^{-2}$, respectively, which is much better than that of the Pt/C catalyst in 1 M phosphate buffer solution (PBS, pH 7). Most impressively, the 3D-Ni/ZnO catalyst demonstrated excellent stability at both 10 and 200 mA cm $^{-2}$ for 2000 h.

■ RESULTS AND DISCUSSION

HER Performance for Ni/MO_x Catalysts. Although different metal/metal oxide heterostructures, such as Ni/NiO and Co/CoO_x catalysts, 26,29,40,41 have been reported to accelerate the water dissociation step for HER, how the oxophilic metal oxides affect their HER activities is not wellunderstood. Different Ni/MO_x (M = Ti, Cr, Mn, Ni, Zn, Cd, or In) heterostructure catalysts were fabricated as the typical example to investigate the effect of MO_x on their HER activities (Figure 1a). We first synthesized the Ni(OH)2 precursor through a simple hydrothermal method (Figures S1 and S2) and then obtained metallic Ni nanoparticles by a thermal reduction process (Figure S3). Subsequently, Ni nanoparticles were mixed with different metal salt precursors with Ni/M molar ratios of 9/1, which were further annealed at 350 °C under an argon atmosphere to generate these Ni/MO_x catalysts. During the annealing treatment, Ni kept its metallic state, while metal salt precursors were thermally decomposed to produce the corresponding MO_x species.

Transmission electron microscopy (TEM) images (Figure S3) showed that bare Ni has a nanoparticle morphology with a

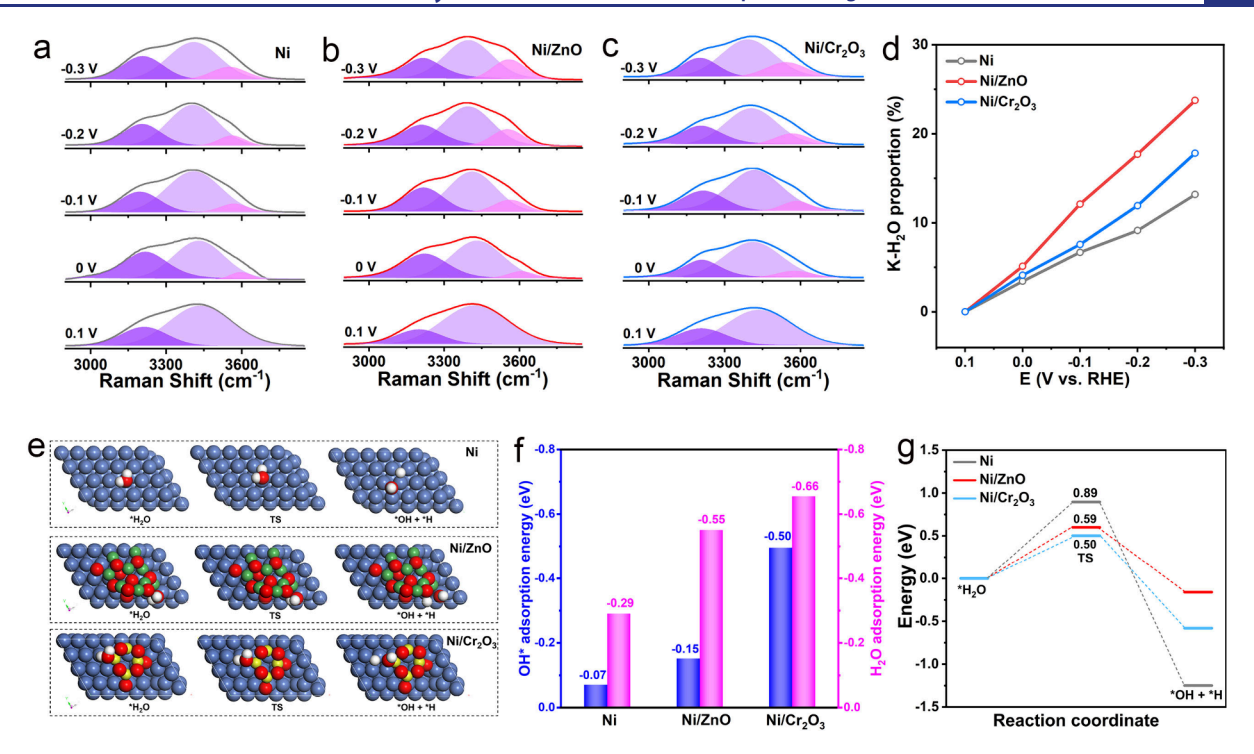


Figure 2. In-situ Raman spectra and DFT calculations. (a-c) In-situ Raman spectra for Ni (a), Ni/ZnO (b), and Ni/Cr₂O₃ (c) catalysts at different cathodic potentials. (d) The proportion of K·H₂O configuration for Ni, Ni/ZnO, and Ni/Cr₂O₃ catalysts at different cathodic potentials. (e) The simulated water dissociation process on Ni(111), Ni/ZnO, and Ni/Cr₂O₃ surfaces. The red, white, blue, green, and yellow spheres represent the O, H, Ni, Zn, and Cr atoms, respectively. (f) The hydroxyl and water adsorption energies on different catalyst surfaces. (g) The energy barriers for water dissociation on different catalyst surfaces.

smooth surface. After the decoration of different MO_x on Ni, the rough surfaces with small MO_x nanoparticles were observed on all Ni/MO_x catalysts. High-resolution TEM (HRTEM) images and energy-dispersive X-ray spectroscopy (EDS) elemental mappings (Figures S4 and S5) revealed the successful formation of the Ni/MO_x heterostructure. X-ray diffraction (XRD) patterns (Figure S6) revealed that the diffraction peaks for the Ni/MO_x catalysts could be well-indexed to the cubic Ni phase. No or weak MO_x phases were found in the XRD results, probably due to the low content and poor crystallinity of the MO_x . We further performed X-ray photoelectron spectroscopy (XPS) characterization to probe the chemical states of the M^{2x+} cation and confirm the composition of MO_x for different Ni/MO_x samples (Figure S7).

Then we systematically evaluated the HER activities of Ni and Ni/MO, catalysts using a typical three-electrode system in 1 M PBS (pH 7). The HER polarization curves showed that coupling Ni with different MO_x concentrations could improve the HER activity of Ni (Figure 1b). Especially, Ni/ZnO exhibited the best HER activity and required the lowest overpotential of 163 mV to reach a current density of 10 mA cm⁻², much better than that of 323 mV for a pure Ni catalyst (Figure 1c). The comparison of mass activities revealed a similar trend for different catalysts (Figure S8). Tafel analysis (Figure S9) revealed that a high slope of ~140 mV dec⁻¹ for pure Ni catalyst implies the Volmer step as the ratedetermining step. 25,28 The decreased slopes for Ni/MO_x catalysts (88-115 mV dec⁻¹) indicate a more efficient Volmer-Heyrovsky mechanism behind them, further confirming the accelerated HER process by oxophilic MOx. In addition, the HER activities for Ni/ZnO with different Ni/Zn ratios were optimized (Figure S10).

The above results demonstrate that the incorporation of oxophilic MO_x on Ni could boost the HER activity, which is governed by the enhanced OHBE. These $\mathrm{Ni/MO}_x$ catalysts prepared by a similar method provide us an opportunity to systematically investigate it and establish a proper HER activity descriptor, thus, aiming for the design of more active HER catalysts in neutral media.

Based on the classic hard and soft acid-base theory, the M^{2x+} cation in MO_x is the Lewis acid site, and its Lewis acidity can reflect the binding ability between metal cations and hydroxyl. We quantified the Lewis acidity of Ni/MO_x catalysts via a commonly used temperature-programmed desorption of ammonia (NH3-TPD) method, which is related to the binding strength between the Lewis acid site and the adsorbed NH3 molecule. 42-45 As shown in Figure 1d, the obtained NH₃-TPD curves have two desorption peak regions, including the weak Lewis acid sites at low temperature (50-300 °C) and the strong acid sites at high temperature (300-600 °C). The integral area of these two regions can reflect the total number of Lewis acidic sites, which are used to represent the Lewis acidity of a catalyst in our study. 42-44 We first gained a small Lewis acidity of 0.084 mmol g⁻¹ for a pure Ni catalyst, which could be attributed to a slight NH3 adsorption from the inevitable oxidation on the Ni surface. Compared with Ni catalyst, all Ni/MO_x composite catalysts exhibited increased Lewis acidity, on account of the increased NH3 adsorption from the MO_x component. As Cr³⁺ and Ti⁴⁺ are known as classic hard Lewis acids, 46,47 Ni/Cr₂O₃ and Ni/TiO₂ showed the high Lewis acidity of 0.63 and 0.53 mmol g^{-1} , respectively, larger than other Ni/MO_x composite catalysts.

We then plotted the experimentally measured Lewis acidity of $\rm Ni/MO_x$ as a function of their HER overpotentials at 10 mA cm⁻² and mass activities at 200 mV overpotential and found a

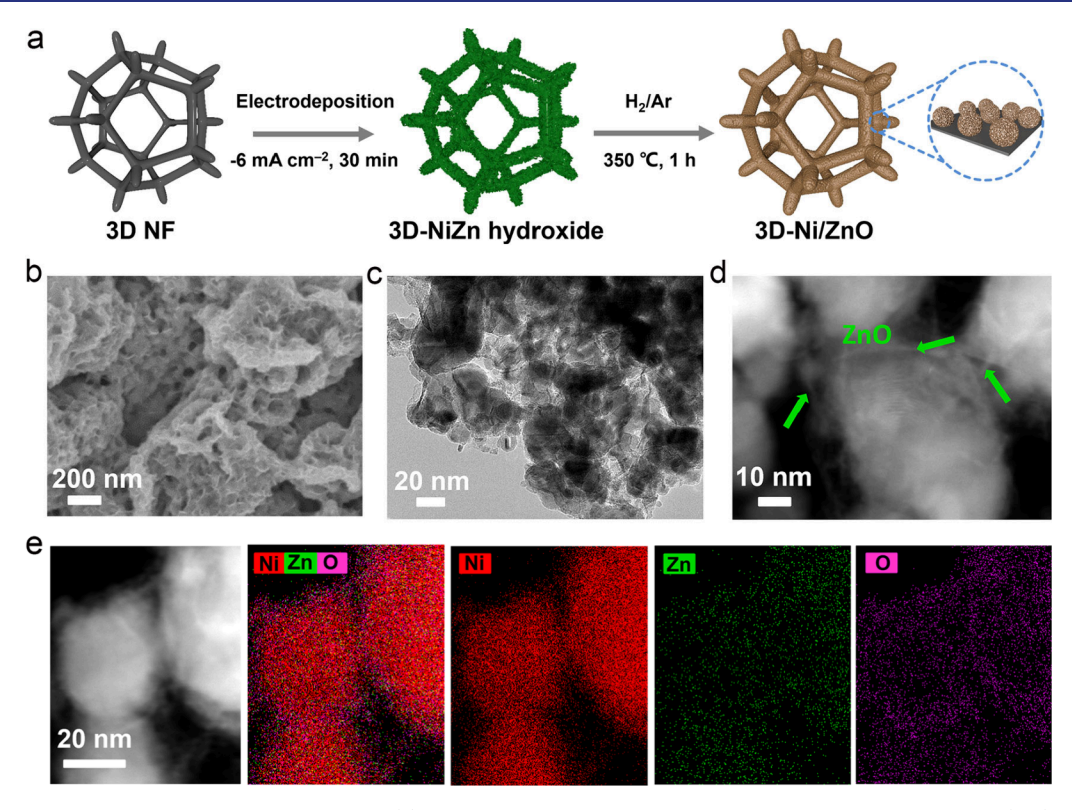


Figure 3. Synthesis and characterization of 3D-Ni/ZnO. (a) Schematic illustration of the synthesis process of 3D-Ni/ZnO. (b-d) SEM, TEM, and STEM images of 3D-Ni/ZnO. The ultrathin ZnO nanoflakes are marked by the green arrows in (d). (e) EDS elemental mappings of 3D-Ni/ZnO.

volcano-type trend between them (Figures 1e and S11). On the left branch of the volcano, Ni and Ni/CdO have weak Lewis acidity, resulting in the weak OH* binding ability and the tough cleavage of H-OH bonds for water dissociation. By contrast, Ni/Cr₂O₃ and Ni/TiO₂ on the right branch with the strong OH* binding ability could expedite the water dissociation step but might inhibit the OH* desorption and thus poison the active sites for readsorption of water. Most impressively, Ni/ZnO located at the top of the volcano has the optimum OH* binding ability to balance water dissociation and OH* desorption, thereby achieving the best HER activity. This volcano relation follows the Sabatier principle, which reflects that the interaction between the catalysts and the adsorbate is neither too weak nor too strong, 48,49 suggesting that the Lewis acidity could be an effective HER activity descriptor for Ni/MO_x catalysts in neutral electrolyte. The Lewis acidity proposed here might be a general activity descriptor to guide the design of other heterostructure catalysts to promote the water dissociation step for efficient HER.

In-Situ Spectroscopy Characterization and DFT Calculations. To further confirm the promoted HER kinetics by the Ni/ZnO catalyst with the optimum OH* binding ability, we conducted in situ spectroscopy characterization and DFT calculations. Ni and Ni/Cr₂O₃ were also compared as the control samples with weak and strong OH* binding ability, respectively. We first performed in situ Raman spectra for Ni, Ni/ZnO, and Ni/Cr₂O₃ catalysts at different cathodic potentials to uncover the change of interfacial water configuration during HER. As shown in Figure 2a-c, all Raman spectra exhibited broad bands at wavenumbers from 3000 to 3800 cm⁻¹, corresponding to the O–H stretching mode of interfacial water. Gaussian fitting of the O–H stretching band can result in three distinct regions, ^{50–52}

including 4-coordinated hydrogen-bonded water at ~3200 cm⁻¹, 2-coordinated hydrogen-bonded water at ~3400 cm⁻¹, and weak hydrogen-bonded cation hydrated water (denoted as $K \cdot H_2O$, K^+ ion is the electrolyte cation) at ~3600 cm⁻¹. According to the previous experimental results and ab initio molecular dynamics simulations, 50 the transformation of interfacial water from a disordered distribution to an ordered structure could be attributed to the formation of the crucial K-H₂O configuration, which can promote the charge transfer efficiency for the facilitated water dissociation. As the cathodic potentials decreased, the K·H₂O proportion (based on the peak area⁵⁰) for all catalysts gradually increased (Figure 2d), on account of the electrostatic effect of the K⁺ ion migrating to the catalyst surface. Compared with Ni and Ni/Cr₂O₃ catalysts, Ni/ZnO exhibits a prominently higher K·H₂O proportion at all applied potentials (Figure 2d), suggesting the more ordered interfacial water induced by the Ni/ZnO catalyst. A lower K·H₂O proportion for Ni/Cr₂O₃ relative to Ni/ZnO could be attributed to the strong OH* binding on the Ni/Cr₂O₃ surface to impede the water adsorption.

DFT calculations were used to further gain a mechanistic understanding of the boosted HER activity for the Ni/ZnO catalyst. We constructed three model surfaces of Ni(111), Ni/ZnO, and Ni/Cr₂O₃ to determine the difference in OH*/H₂O adsorption as well as the water dissociation (Figures 2e, S12, and S13). As proven by the above NH₃-TPD experiments (Figure 1d), the coupling of Ni with the oxophilic metal oxides can enhance the OH* adsorption to varying degrees. It is also confirmed by the calculated results that the OH* adsorption energies for Ni/ZnO and Ni/Cr₂O₃ are -0.15 and -0.50 eV, respectively, more negative than that of -0.07 eV for pure Ni (Figure 2f). The strong OH* adsorption can facilely promote water adsorption on the catalyst surface. As a result, compared

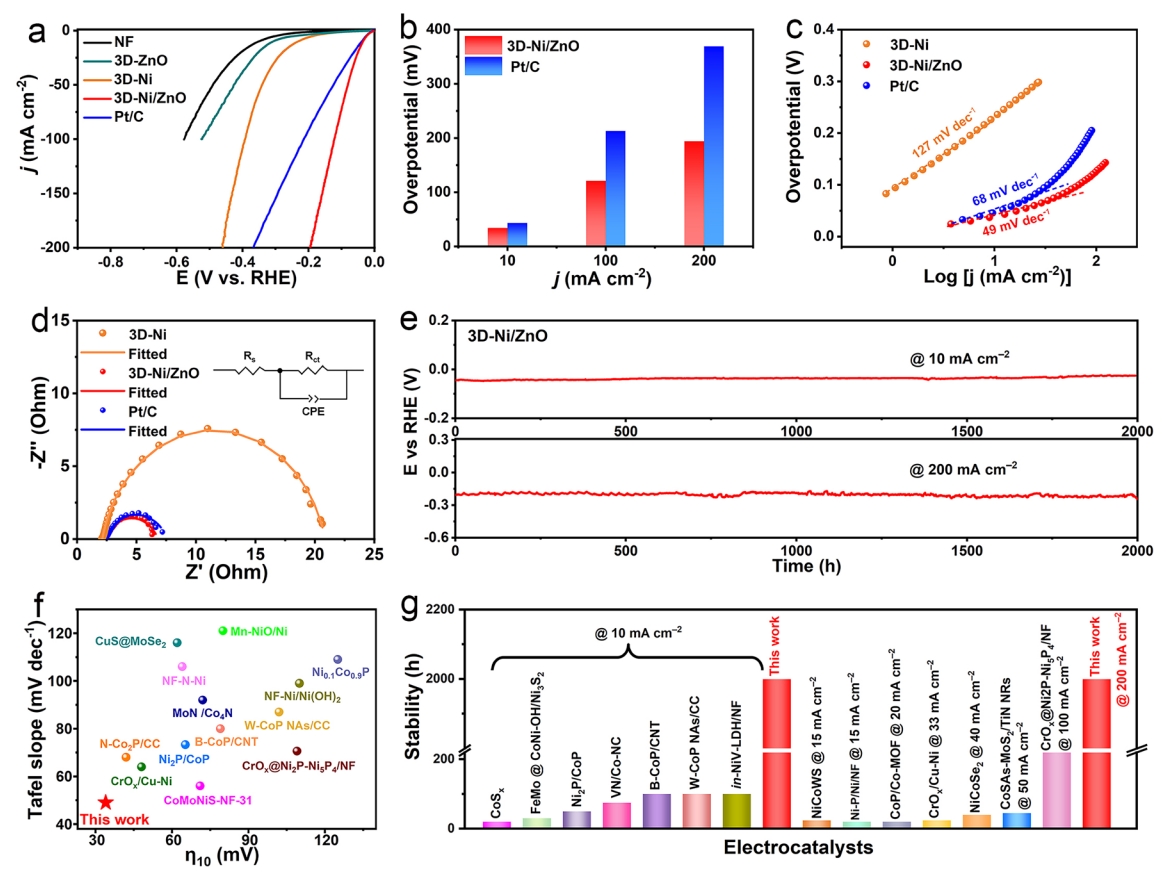


Figure 4. Electrocatalytic HER performance for 3D-Ni/ZnO in neutral electrolyte. (a) HER polarization curves with *iR* correction for different catalysts in 1 M PBS. Scan rate: 2 mV s⁻¹. (b) Comparison of the required overpotentials for 3D-Ni/ZnO and Pt/C catalysts at different current densities. (c) Tafel plots for different catalysts. (d) EIS Nyquist plots for different catalysts at a 100 mV overpotential. (e) Chronopotentiometric curves for 3D-Ni/ZnO at 10 and 200 mA cm⁻². (f) Comparison of HER overpotentials and Tafel slopes for 3D-Ni/ZnO and other reported neutral HER catalysts. (g) Comparison of stability time for 3D-Ni/ZnO and other reported neutral HER catalysts.

with pure Ni surface, Ni/ZnO and Ni/Cr₂O₃ have a stronger water adsorption (Figure 2f). We further calculated the energy barriers for water dissociation on different catalyst surfaces (Figure 2g). The Ni catalyst with weak OH*/H₂O adsorption shows a very high water dissociation energy of 0.89 eV, which is responsible for its sluggish HER kinetics and poor HER activity. 25,27 In contrast, Ni/ZnO and Ni/Cr₂O₃ can favor the water dissociation step by binding with OH* on the oxide site and H* on the Ni site to expedite the cleavage of H-OH bonds. Therefore, low energy barriers for water dissociation are observed on Ni/ZnO (0.59 eV) and Ni/Cr₂O₃ (0.50 eV), indicating the promoted water dissociation on them. Nevertheless, Ni/Cr₂O₃ exhibits a much stronger OH* adsorption than Ni/ZnO (Figure 2f), which will hinder the OH* desorption and water readsorption on Ni/Cr2O3 surface, thereby leading to a worse HER activity for Ni/Cr₂O₃ relative to Ni/ZnO. These theoretical results are consistent with the above volcano trend (Figure 1e), again verifying that Ni/ZnO catalyst with the moderate OH* binding ability can balance the water dissociation and OH* desorption to deliver the best HER activity.

Synthesis and Characterization of 3D-Ni/ZnO Catalyst. Motivated by the optimum composition of active Ni/ZnO from the above experimental and theoretical results, we sought to construct the Ni/ZnO heterostructure catalyst on a three-dimensional Ni foam (3D-NF) substrate to expose more active sites and thereby to improve the HER performance

(Figure 3a). We first in situ grew NiZn-based hydroxide on 3D-NF through an electrochemical codeposition method (Figures S14–S16). Afterward, the hydroxide precursor was thermally annealed in an $\rm H_2/Ar$ atmosphere at 350 °C to directly produce a 3D-Ni/ZnO catalyst. During the thermal reduction process, Ni-based hydroxide was reduced to metallic Ni and Zn-based hydroxide was converted into ZnO phase. We can easily obtain a large-sized 3D-Ni/ZnO electrode with an area of 2 \times 14 cm² (Figure S17), indicating a good scalability for this simple synthetic method.

Scanning electron microscopy (SEM) images of 3D-Ni/ ZnO (Figures 3b and S17) showed that plenty of Ni/ZnO nanoflakes were loaded onto the 3D-NF skeleton. As imaged by TEM and scanning TEM (Figures 3c,d and S17), Ni/ZnO was composed of Ni nanoparticles covered by ultrathin ZnO nanoflakes. EDS elemental mappings (Figure 3e) further revealed that the ZnO nanoflakes were uniformly coated on the surface of the Ni nanoparticles. The Ni/Zn molar ratio for Ni/ZnO was determined to be ~9/1 from inductively coupled plasma mass spectroscopy (ICP-MS) measurement, similar to the initial feed ratio in the electrodeposition process. We also synthesized 3D-Ni/ZnO with other Ni/Zn ratios by adjusting the initial feed ratios (Figures S18 and S19). In addition, pure Ni and ZnO samples grown on a 3D-NF substrate (denoted as 3D-Ni and 3D-ZnO, respectively) were also prepared through a similar method (Figures S20 and S21).

HER Performance for 3D-Ni/ZnO Catalyst. We then investigated the HER performance for the 3D-Ni/ZnO catalyst and other control samples in 1 M PBS. Commercial Pt/C (20 wt %) catalyst coated on 3D-NF with Nafion binder was also tested for comparison. Figure 4a shows the typical HER polarization curves for different samples. 3D-ZnO exhibited the approximate polarization curve with the 3D-NF substrate, indicating the poor HER activity for ZnO. 3D-Ni can moderately improve HER activity with an overpotential of 231 mV at a current density of 10 mA cm⁻². Most impressively, 3D-Ni/ZnO showed outstanding HER activity (Figures 4b and S22), which requires small overpotentials of 34, 121, and 194 mV to reach the current densities of 10, 100, and 200 mA cm⁻², respectively. It outperformed the Pt/C catalyst with 43, 213, and 369 mV overpotentials to achieve the corresponding current densities. The overpotential of 43 mV at 10 mA cm⁻² for Pt/C catalyst is close to many reported Pt/C catalysts in the literatures. 14,21,53-55 It is remarkable that 3D-Ni/ZnO shows significantly lower HER overpotentials than that for Pt/C at large current densities (>100 mA cm⁻²), indicating the prominent benefit of the in situ growth of active Ni/ZnO component on the 3D conductive substrate. It was probably due to the blockage of some Pt/C active sites by binder polymer, thus leading to the poor mass transfer. 21,23,2

Tafel slope analysis gave values of 127, 49, and 68 mV dec⁻¹ for 3D-Ni, 3D-Ni/ZnO, and Pt/C, respectively (Figure 4c). Compared with 3D-Ni, the decreased Tafel slope for 3D-Ni/ZnO implies that the HER mechanism shifts from the Volmer rate-determining step to Volmer—Heyrovsky mechanism. We further carried out the electrochemical impedance spectroscopy (EIS) tests and found that 3D-Ni/ZnO catalyst had the smallest charge transfer resistance of \sim 4 Ω (Figure 4d), indicating the fastest charge transfer kinetics. The evolved hydrogen amount was detected via gas chromatography, yielding approximately 100% Faradaic efficiency for 3D-Ni/ZnO catalyst (Figure S23). We also optimized the Ni/Zn molar ratio and found that 3D-Ni/ZnO with a Ni/Zn molar ratio of 9/1 had the best HER activity (Figure S24).

Apart from the catalytic activity, long-term stability is another vital metric for catalyst evaluation. We thus performed chronopotentiometry tests at constant current densities of 10 and 200 mA cm⁻² to examine the HER durability. The voltage—time curves in Figure 4e demonstrate that 3D-Ni/ZnO could stably operate at both 10 and 200 mA cm⁻² for >2000 h without any degradation. The post-mortem characterizations displayed the robust morphology and structure for 3D-Ni/ZnO after HER stability tests (Figures S25—S27). In terms of the overpotential, Tafel slope, and stability time, our 3D-Ni/ZnO surpasses most of the reported neutral HER catalysts, representing the best active and durable HER catalysts in neutral electrolyte (Figure 4f,g and Table S1).

CONCLUSION

In summary, we found a volcano-like relationship between the HER activity and Lewis acidity of Ni/MO_x heterostructure catalysts and proposed Lewis acidity as an effective activity descriptor for Ni/MO_x-based catalysts in a neutral electrolyte. Especially, Ni/ZnO located at the top of the volcano has the optimum OH* binding ability to balance the water dissociation and OH* desorption, thereby achieving the best HER activity. Based on our finding, we further constructed the active Ni/ZnO component on the 3D conductive substrate to expose more active sites. As a result, the obtained 3D-Ni/ZnO

can efficiently and robustly catalyze the HER in 1 M PBS, greatly exceeding other reported neutral HER catalysts in the literature. The outstanding HER activity and durability for our developed catalyst reveal the rational design strategy for the achievement of active and nonprecious HER catalysts in neutral electrolyte.

■ EXPERIMENTAL SECTION

Synthesis of Ni/MO_x. We first prepared Ni nanoparticles through a simple hydrothermal method, followed by a thermal reduction process. Briefly, 2 mmol of Ni(NO₃)₂·6H₂O, 10 mmol of urea, and 30 mL of water were mixed and transferred into a 50 mL Teflon-lined stainless autoclave at 120 °C for 6 h. After centrifugation and washing, the resulting Ni(OH)₂ precursor was annealed in an H₂/Ar atmosphere at 350 °C for 1 h to produce the Ni nanoparticles. Then MO_x (M = Ti, Cr, Mn, Ni, Zn, Cd, or In) was decorated on Ni nanoparticles through a thermodecomposition method. Different metal salt precursors (0.1 mmol), including $Ti(OC_4H_9)_4$, $Cr(CH_3COO)_3$, $Mn(CH_3COO)_2$, $Ni(CH_3COO)_2$, $Zn(CH_3COO)_2$, $Cd(CH_3COO)_2$, or $In(CH_3COO)_3$, were dissolved in ethanol and mixed with 0.9 mmol of Ni nanoparticles, which were annealed at 350 °C in an argon atmosphere to produce different Ni/MO_x samples.

Synthesis of 3D-Ni/ZnO. The 3D-Ni/ZnO electrode was prepared through an in situ electrodeposition method, followed by a thermal treatment process. Typically, Ni/Zn hydroxide was electrodeposited on the Ni foam substrate $(1 \times 2.5 \text{ cm}^2)$ at a constant current density of -6 mA cm⁻² for 30 min in a mixed aqueous solution (50 mL) of 45 mM of Ni(NO₃)₂·6H₂O and 5 mM Zn(NO₃)₂·6H₂O with Ni/Zn molar ratio of 9/1. The resulting electrode was rinsed with deionized water and ethanol to remove the unstable sediments, and the mixture was further annealed in a H₂/Ar atmosphere at 350 °C for 1 h to produce the 3D-Ni/ZnO electrode. We can easily obtain the electrode with a larger size $(2 \times 14 \text{ cm}^2)$ by simply increasing the electrode area, and we kept the same solution concentration but increased the solution volume to 200 mL. For comparison, 3D-Ni or 3D-ZnO was prepared through the similar method but without adding Zn(NO₃)₂·6H₂O or Ni(NO₃)₂·6H₂O during the electrodeposition.

Material Characterizations. Powder XRD patterns were taken on an X-ray diffractometer (Japan Rigaku SmartLab 9 KW) with Cu $K\alpha$ radiation (λ = 1.5418 Å). SEM images were carried out on a scanning electron microscope (FEI Verios 460L). TEM and EDS elemental mapping images were obtained from a transmission electron microscope (FEI Talos F200X). XPS spectra were recorded on an ESCALAB250Xi spectrometer (Thermo Scientific) with Al K α radiation. ICP-MS measurements were carried out with a Thermo Scientific iCAP RQ instrument. In-situ Raman spectra were taken on a LabRAM HR Evolution Confocal Raman Microscope (HORIBA JY), which were first performed at different applied potentials for 5 min and then were recorded. NH₃-TPD was carried out on a multifunctional automatic adsorption instrument (AUTO CHEM 2920). Before NH₃ adsorption, the sample was first treated at 300 °C for 1 h in a He atmosphere. After the adsorption of NH3 at 50 °C for 1 h, the NH₃ desorption process was performed from 50 to 700 °C at a heating rate of 10 °C min⁻¹.

Electrochemical Measurements. The electrocatalytic HER measurements for different samples were carried out via a typical three-electrode system in an electrochemical workstation (CHI 760E, Shanghai Chenhua) at room temperature. The electrolyte is 1 M PBS (pH 7). Different Ni/MO_x catalysts (\sim 2.0 mg cm⁻²) coated on NF (1 × 1 cm²) with 10% Nafion binder were used as the working electrode. 3D-Ni/ZnO with active mass loading of 2.5 mg cm⁻² was used directly as the working electrode. For comparison, commercial Pt/C (20 wt %, Johnson Matthey) with loading of 2.5 mg cm⁻² on 3D-NF was also tested. The Ag/AgCl (3.5 M KCl) electrode and graphite rod electrode were used as the reference and counter electrodes, respectively. The potential used against the Ag/AgCl electrode was converted to the reversible hydrogen electrode (RHE) scale using $E_{RHE} = E_{Ae/AeCl} + 0.059 \text{ pH} + 0.196 \text{ V}$. The HER polarization curves

were recorded at a scan rate of 2 mV s⁻¹. The EIS tests were carried out under the frequencies ranging from $10^{5}\ \text{to}\ 0.1\ \text{Hz}$ with a voltage amplitude of 5 mV at an applied potential of -0.1 V versus RHE. The long-term stability for the 3D-Ni/ZnO catalyst was examined via a chronopotentiometry method at constant current densities of 10 and 200 mA cm⁻². All the potentials here were reported with iR-correction unless otherwise stated.

DFT Calculations. Spin-polarized DFT calculations were performed with the Vienna ab initio simulation package (VASP). 56,57 The generalized gradient approximation (GGA) of Perdew-Burke-Ernzerhof (PBE)⁵⁸ functional was adopted for the electron exchange-correlation. And the projected augmented wave (PAW) method⁵⁹ was used to describe the electron-ion interaction. During the calculations, the valence states were expanded in a planewave basis set with a cutoff energy of 420 eV and the Ni(3d4s), Cr(3d4s), Zn(3d4s), O(2s2p), and H(1s) electrons were treated as the valence states.

Ni(111) surface was modeled with four layers of slab in (4×6) lateral cells. During the calculations, the top two layers were relaxed, and the bottom two layers were frozen. For Ni(111)/ZnO and Ni(111)/Cr₂O₃, ZnO and Cr₂O₃ clusters are loaded on the Ni(111) surface. A 15 Å vacuum layer was set to the three computational model to avoid the interaction between two adjacent layers. And the Brillouin zone was sampled by a Monkhorst-Pack mesh with a 2 × 2 × 1 grid in the reciprocal space. To balance the computational cost and accuracy, the convergence tolerance was set to 10^{-5} eV for energy variation and 0.02 eV/ Å for force on each atom. The climbing-image nudged elastic band (CI-NEB) method⁶⁰ was used to search the transition states (TS) of the water splitting on the three computational models. To verify the obtained TS structures, vibrational frequency analysis was conducted. For each TS structure, only one imaginary frequency over the reaction coordinate existed.

The activation energy for the water dissociation was computed by $\Delta E_{\rm a} = E_{\rm TS} - E_{\rm IS}$, where $E_{\rm TS}$ represents the energy of the transition state (TS) and E_{IS} represents the energy of the corresponding initial state (IS). The absorption energy for OH* was calculated by $\Delta E_{\rm OH}$ = $E_{OH+slab}$ - E_{slab} - E_{H2O} + 0.5 E_{H2} , where $E_{OH+slab}$ and E_{slab} represent the energies of the surfaces with and without OH adsorbate, respectively, E_{H2O} is the energy of a H₂O molecule, and E_{H2} is the energy of a H₂ molecule. The absorption energy for H₂O was calculated by $\Delta E_{\rm H2O}$ = $E_{\rm H2O+slab}$ - $E_{\rm slab}$ - $E_{\rm H2O}$, where $E_{\rm H2O+slab}$ and E_{slab} represent the energies of the surfaces with and without H₂O adsorbate, respectively, and $E_{\rm H2O}$ is the energy of a H_2O molecule.

ASSOCIATED CONTENT

Supporting Information

The Supporting Information is available free of charge at https://pubs.acs.org/doi/10.1021/jacs.4c16596.

Morphological and structural characterizations for Ni, Ni/MO_x, 3D-Ni/ZnO, and other control samples; additional electrocatalytic data for all samples; and DFT calculation models (PDF)

AUTHOR INFORMATION

Corresponding Authors

Zi-You Yu – MOE International Joint Laboratory of Materials Microstructure, Institute for New Energy Materials and Low Carbon Technologies, School of Materials Science & Engineering, Tianjin University of Technology, Tianjin 300384, China; orcid.org/0000-0002-8932-0814; Email: yuziyou@email.tjut.edu.cn

Tong-Bu Lu - MOE International Joint Laboratory of Materials Microstructure, Institute for New Energy Materials and Low Carbon Technologies, School of Materials Science & Engineering, Tianjin University of Technology, Tianjin

300384, China; orcid.org/0000-0002-6087-4880; Email: lutongbu@tjut.edu.cn

Authors

Lin-Lin Wang – MOE International Joint Laboratory of Materials Microstructure, Institute for New Energy Materials and Low Carbon Technologies, School of Materials Science & Engineering, Tianjin University of Technology, Tianjin 300384, China

Xiao-Ran Wang - MOE International Joint Laboratory of Materials Microstructure, Institute for New Energy Materials and Low Carbon Technologies, School of Materials Science & Engineering, Tianjin University of Technology, Tianjin 300384, China

Hong-Juan Wang – MOE International Joint Laboratory of Materials Microstructure, Institute for New Energy Materials and Low Carbon Technologies, School of Materials Science & Engineering, Tianjin University of Technology, Tianjin 300384, China

Chong Zhang – The Instruments Center for Physical Science, University of Science and Technology of China, Hefei 230026, China

Jing-Jing Li – MOE International Joint Laboratory of Materials Microstructure, Institute for New Energy Materials and Low Carbon Technologies, School of Materials Science & Engineering, Tianjin University of Technology, Tianjin 300384, China

Guo-Jin Feng – MOE International Joint Laboratory of Materials Microstructure, Institute for New Energy Materials and Low Carbon Technologies, School of Materials Science & Engineering, Tianjin University of Technology, Tianjin 300384, China

Xuan-Xuan Cheng – MOE International Joint Laboratory of Materials Microstructure, Institute for New Energy Materials and Low Carbon Technologies, School of Materials Science & Engineering, Tianjin University of Technology, Tianjin 300384, China

Xue-Rong Qin – MOE International Joint Laboratory of Materials Microstructure, Institute for New Energy Materials and Low Carbon Technologies, School of Materials Science & Engineering, Tianjin University of Technology, Tianjin 300384, China

Complete contact information is available at: https://pubs.acs.org/10.1021/jacs.4c16596

Author Contributions

§(L.-L.W., X.-R.W., H.-J.W., C.Z.) These authors contributed equally to this work.

Notes

The authors declare no competing financial interest.

ACKNOWLEDGMENTS

This work was supported by National Key R&D Program of China (2022YFA1502902) and National Natural Science Foundation of China (21931007, 22375146, and 22109149).

REFERENCES

(1) Shi, Z.; Zhang, X.; Lin, X.; Liu, G.; Ling, C.; Xi, S.; Chen, B.; Ge, Y.; Tan, C.; Lai, Z.; Huang, Z.; Ruan, X.; Zhai, L.; Li, L.; Li, Z.; Wang, X.; Nam, G.-H.; Liu, J.; He, Q.; Guan, Z.; Wang, J.; Lee, C.-S.; Kucernak, A. R. J.; Zhang, H. Phase-dependent growth of Pt on MoS₂ for highly efficient H₂ evolution. *Nature* **2023**, 621, 300–305.

- (2) Turner, J. A. Sustainable hydrogen production. *Science* **2004**, 305, 972–974.
- (3) Yu, Z.-Y.; Duan, Y.; Feng, X.-Y.; Yu, X.; Gao, M.-R.; Yu, S.-H. Clean and Affordable Hydrogen Fuel from Alkaline Water Splitting: Past, Recent Progress, and Future Prospects. *Adv. Mater.* **2021**, *33*, 2007100.
- (4) Ram, R.; Xia, L.; Benzidi, H.; Guha, A.; Golovanova, V.; Garzón Manjón, A.; Llorens Rauret, D.; Sanz Berman, P.; Dimitropoulos, M.; Mundet, B.; Pastor, E.; Celorrio, V.; Mesa, C. A.; Das, A. M.; Pinilla-Sánchez, A.; Giménez, S.; Arbiol, J.; López, N.; García de Arquer, F. P. Water-hydroxide trapping in cobalt tungstate for proton exchange membrane water electrolysis. *Science* **2024**, *384*, 1373–1380.
- (5) Zou, X.; Zhang, Y. Noble metal-free hydrogen evolution catalysts for water splitting. *Chem. Soc. Rev.* **2015**, *44*, 5148–5180.
- (6) Lagadec, M. F.; Grimaud, A. Water electrolysers with closed and open electrochemical systems. *Nat. Mater.* **2020**, *19*, 1140–1150.
- (7) Zhang, X.-L.; Yu, P.-C.; Su, X.-Z.; Hu, S.-J.; Shi, L.; Wang, Y.-H.; Yang, P.-P.; Gao, F.-Y.; Wu, Z.-Z.; Chi, L.-P.; Zheng, Y.-R.; Gao, M.-R. Efficient acidic hydrogen evolution in proton exchange membrane electrolyzers over a sulfur-doped marcasite-type electrocatalyst. *Sci. Adv.* 2023, *9*, No. eadh2885.
- (8) Zheng, X.; Shi, X.; Ning, H.; Yang, R.; Lu, B.; Luo, Q.; Mao, S.; Xi, L.; Wang, Y. Tailoring a local acid-like microenvironment for efficient neutral hydrogen evolution. *Nat. Commun.* **2023**, *14*, 4209.
- (9) Zhang, B.; Wang, J.; Liu, G.; Weiss, C. M.; Liu, D.; Chen, Y.; Xia, L.; Zhou, P.; Gao, M.; Liu, Y.; Chen, J.; Yan, Y.; Shao, M.; Pan, H.; Sun, W. A strongly coupled Ru–CrO_x cluster–cluster heterostructure for efficient alkaline hydrogen electrocatalysis. *Nat. Catal.* **2024**, *7*, 441–451.
- (10) Chen, J.; Chen, C.; Qin, M.; Li, B.; Lin, B.; Mao, Q.; Yang, H.; Liu, B.; Wang, Y. Reversible hydrogen spillover in Ru-WO_{3-x} enhances hydrogen evolution activity in neutral pH water splitting. *Nat. Commun.* **2022**, *13*, 5382.
- (11) Dinh, C.-T.; Jain, A.; de Arquer, F. P. G.; De Luna, P.; Li, J.; Wang, N.; Zheng, X.; Cai, J.; Gregory, B. Z.; Voznyy, O.; Zhang, B.; Liu, M.; Sinton, D.; Crumlin, E. J.; Sargent, E. H. Multi-site electrocatalysts for hydrogen evolution in neutral media by destabilization of water molecules. *Nat. Energy* **2019**, *4*, 107–114.
- (12) Kanan, M. W.; Nocera, D. G. In Situ Formation of an Oxygen-Evolving Catalyst in Neutral Water Containing Phosphate and Co²⁺. *Science* **2008**, *321*, 1072–1075.
- (13) Zhou, Z.; Pei, Z.; Wei, L.; Zhao, S.-L.; Jian, X.; Chen, Y. Electrocatalytic Hydrogen Evolution under Neutral pH Conditions: Current Understandings, Recent Advances, and Future Prospects. *Energy Environ. Sci.* **2020**, *13*, 3185–3206.
- (14) Wu, R.; Xiao, B.; Gao, Q.; Zheng, Y.; Zheng, X.; Zhu, J.; Gao, M.-R.; Yu, S.-H. A Janus Nickel Cobalt Phosphide Catalyst for Highefficiency Neutral-pH Water Splitting. *Angew. Chem., Int. Ed.* **2018**, 57, 15445–15449.
- (15) Zhai, L.; She, X.; Zhuang, L.; Li, Y.; Ding, R.; Guo, X.; Zhang, Y.; Zhu, Y.; Xu, K.; Fan, H. J.; Lau, S. P. Modulating Built-In Electric Field via Variable Oxygen Affinity for Robust Hydrogen Evolution Reaction in Neutral Media. *Angew. Chem., Int. Ed.* **2022**, *61*, No. e202116057.
- (16) Morales-Guio, C. G.; Stern, L.-A.; Hu, X. Nanostructured hydrotreating catalysts for electrochemical hydrogen evolution. *Chem. Soc. Rev.* **2014**, *43*, 6555–6569.
- (17) Wei, Z.-W.; Wang, H.-J.; Zhang, C.; Xu, K.; Lu, X.-L.; Lu, T.-B. Reversed Charge Transfer and Enhanced Hydrogen Spillover in Platinum Nanoclusters Anchored on Titanium Oxide with Rich Oxygen Vacancies Boost Hydrogen Evolution Reaction. *Angew. Chem., Int. Ed.* **2021**, *60*, 16622–16627.
- (18) Subbaraman, R.; Tripkovic, D.; Chang, K.-C.; Strmcnik, D.; Paulikas, A. P.; Hirunsit, P.; Chan, M.; Greeley, J.; Stamenkovic, V.; Markovic, N. M. Trends in activity for the water electrolyser reactions on 3d M(Ni,Co,Fe,Mn) hydr(oxy)oxide catalysts. *Nat. Mater.* **2012**, *11*, 550–557.

- (19) Strmcnik, D.; Lopes, P. P.; Genorio, B.; Stamenkovic, V. R.; Markovic, N. M. Design principles for hydrogen evolution reaction catalyst materials. *Nano Energy* **2016**, *29*, 29–36.
- (20) McCrum, I. T.; Koper, M. T. M. The role of adsorbed hydroxide in hydrogen evolution reaction kinetics on modified platinum. *Nat. Energy* **2020**, *5*, 891–899.
- (21) Maji, M.; Dutta, S.; Jena, R.; Dey, A.; Maji, T. K.; Pati, S. K.; Bhattacharyya, S. Hydrogen Evolution in Neutral Media by Differential Intermediate Binding at Charge-Modulated Sites of a Bimetallic Alloy Electrocatalyst. *Angew. Chem., Int. Ed.* **2024**, *63*, No. e202403697.
- (22) Mao, B.; Sun, P.; Jiang, Y.; Meng, T.; Guo, D.; Qin, J.; Cao, M. Identifying the Transfer Kinetics of Adsorbed Hydroxyl as a Descriptor of Alkaline Hydrogen Evolution Reaction. *Angew. Chem., Int. Ed.* **2020**, *59*, 15232–15237.
- (23) Fu, H. Q.; Zhou, M.; Liu, P. F.; Liu, P.; Yin, H.; Sun, K. Z.; Yang, H. G.; Al-Mamun, M.; Hu, P.; Wang, H.-F.; Zhao, H. Hydrogen Spillover-Bridged Volmer/Tafel Processes Enabling Ampere-Level Current Density Alkaline Hydrogen Evolution Reaction under Low Overpotential. J. Am. Chem. Soc. 2022, 144, 6028–6039.
- (24) Gong, M.; Wang, D.-Y.; Chen, C.-C.; Hwang, B.-J.; Dai, H. A mini review on nickel-based electrocatalysts for alkaline hydrogen evolution reaction. *Nano Res.* **2016**, *9*, 28–46.
- (25) Sun, H.; Yan, Z.; Tian, C.; Li, C.; Feng, X.; Huang, R.; Lan, Y.; Chen, J.; Li, C.-P.; Zhang, Z.; Du, M. Bixbyite-type Ln_2O_3 as promoters of metallic Ni for alkaline electrocatalytic hydrogen evolution. *Nat. Commun.* **2022**, *13*, 3857.
- (26) Gong, M.; Zhou, W.; Tsai, M.-C.; Zhou, J.; Guan, M.; Lin, M.-C.; Zhang, B.; Hu, Y.; Wang, D.-Y.; Yang, J.; Pennycook, S. J.; Hwang, B.-J.; Dai, H. Nanoscale nickel oxide/nickel heterostructures for active hydrogen evolution electrocatalysis. *Nat. Commun.* **2014**, *5*, 4695.
- (27) You, B.; Liu, X.; Hu, G.; Gul, S.; Yano, J.; Jiang, D. -e.; Sun, Y. Universal Surface Engineering of Transition Metals for Superior Electrocatalytic Hydrogen Evolution in Neutral Water. *J. Am. Chem. Soc.* 2017, 139, 12283–12290.
- (28) Kim, J.; Jung, H.; Jung, S.-M.; Hwang, J.; Kim, D. Y.; Lee, N.; Kim, K.-S.; Kwon, H.; Kim, Y.-T.; Han, J. W.; Kim, J. K. Tailoring Binding Abilities by Incorporating Oxophilic Transition Metals on 3D Nanostructured Ni Arrays for Accelerated Alkaline Hydrogen Evolution Reaction. J. Am. Chem. Soc. 2021, 143, 1399–1408.
- (29) Zhao, L.; Zhang, Y.; Zhao, Z.; Zhang, Q.-H.; Huang, L.-B.; Gu, L.; Lu, G.; Hu, J.-S.; Wan, L.-J. Steering elementary steps towards efficient alkaline hydrogen evolution via size-dependent Ni/NiO nanoscale heterosurfaces. *Natl. Sci. Rev.* **2020**, *7*, 27–36.
- (30) Chen, Y.; Rao, Y.; Wang, R.; Yu, Y.; Li, Q.; Bao, S.; Xu, M.; Yue, Q.; Zhang, Y.; Kang, Y. Interfacial engineering of Ni/V_2O_3 for hydrogen evolution reaction. *Nano Res.* **2020**, *13*, 2407–2412.
- (31) Ming, M.; Ma, Y.; Zhang, Y.; Huang, L.-B.; Zhao, L.; Chen, Y.-Y.; Zhang, X.; Fan, G.; Hu, J.-S. 3D nanoporous Ni/V₂O₃ hybrid nanoplate assemblies for highly efficient electrochemical hydrogen evolution. *J. Mater. Chem. A* **2018**, *6*, 21452–21457.
- (32) Li, X.; Liu, P. F.; Zhang, L.; Zu, M. Y.; Yang, Y. X.; Yang, H. G. Enhancing alkaline hydrogen evolution reaction activity through Ni–Mn₃O₄ nanocomposites. *Chem. Commun.* **2016**, 52, 10566–10569.
- (33) Li, X.; Wang, Y.; Wang, J.; Da, Y.; Zhang, J.; Li, L.; Zhong, C.; Deng, Y.; Han, X.; Hu, W. Sequential Electrodeposition of Bifunctional Catalytically Active Structures in MoO₃/Ni–NiO Composite Electrocatalysts for Selective Hydrogen and Oxygen Evolution. *Adv. Mater.* **2020**, *32*, 2003414.
- (34) Danilovic, N.; Subbaraman, R.; Strmcnik, D.; Chang, K.-C.; Paulikas, A. P.; Stamenkovic, V. R.; Markovic, N. M. Enhancing the Alkaline Hydrogen Evolution Reaction Activity through the Bifunctionality of Ni(OH)₂/Metal Catalysts. *Angew. Chem., Int. Ed.* **2012**, *51*, 12495–12498.
- (35) Dai, L.; Chen, Z.-N.; Li, L.; Yin, P.; Liu, Z.; Zhang, H. Ultrathin Ni(0)-Embedded Ni(OH)₂ Heterostructured Nanosheets with Enhanced Electrochemical Overall Water Splitting. *Adv. Mater.* **2020**, 32, 1906915.

- (36) Chhetri, M.; Sultan, S.; Rao, C. Electrocatalytic hydrogen evolution reaction activity comparable to platinum exhibited by the Ni/Ni(OH)₂/graphite electrode. *Proc. Natl. Acad. Sci. U. S. A.* **2017**, 114, 8986–8990.
- (37) Wu, Z.; Wang, Z.; Geng, F. Radially Aligned Hierarchical Nickel/Nickel-Iron (Oxy)hydroxide Nanotubes for Efficient Electrocatalytic Water Splitting. ACS Appl. Mater. Interfaces 2018, 10, 8585–8593.
- (38) Zhang, J.; Chen, G.; Liu, Q.; Fan, C.; Sun, D.; Tang, Y.; Sun, H.; Feng, X. Competitive Adsorption: Reducing the Poisoning Effect of Adsorbed Hydroxyl on Ru Single-Atom Site with SnO2 for Efficient Hydrogen Evolution. *Angew. Chem., Int. Ed.* **2022**, *61*, No. e202209486.
- (39) Zeng, Z.; Chang, K.-C.; Kubal, J.; Markovic, N. M.; Greeley, J. Stabilization of ultrathin (hydroxy)oxide films on transition metal substrates for electrochemical energy conversion. *Nat. Energy* **2017**, *2*, 17070
- (40) Jin, H.; Wang, J.; Su, D.; Wei, Z.; Pang, Z.; Wang, Y. In situ Cobalt—Cobalt Oxide/N-Doped Carbon Hybrids As Superior Bifunctional Electrocatalysts for Hydrogen and Oxygen Evolution. *J. Am. Chem. Soc.* **2015**, *137*, 2688–2694.
- (41) Yan, X.; Tian, L.; He, M.; Chen, X. Three-Dimensional Crystalline/Amorphous Co/Co₃O₄ Core/Shell Nanosheets as Efficient Electrocatalysts for the Hydrogen Evolution Reaction. *Nano Lett.* **2015**, *15*, 6015–6021.
- (42) Yang, Q.; Xu, W.; Gong, S.; Zheng, G.; Tian, Z.; Wen, Y.; Peng, L.; Zhang, L.; Lu, Z.; Chen, L. Atomically dispersed Lewis acid sites boost 2-electron oxygen reduction activity of carbon-based catalysts. *Nat. Commun.* **2020**, *11*, 5478.
- (43) Mekki-Berrada, A.; Grondin, D.; Bennici, S.; Auroux, A. Design of amphoteric mixed oxides of zinc and Group 3 elements (Al, Ga, In): migration effects on basic features. *Phys. Chem. Chem. Phys.* **2012**, 14, 4155–4161.
- (44) Sun, J.; Baylon, R. A. L.; Liu, C.; Mei, D.; Martin, K. J.; Venkitasubramanian, P.; Wang, Y. Key Roles of Lewis Acid—Base Pairs on Zn_xZr_yO_z in Direct Ethanol/Acetone to Isobutene Conversion. *J. Am. Chem. Soc.* **2016**, *138*, 507–517.
- (45) Dong, G. -j.; Zhang, Y. -f.; Zhao, Y.; Bai, Y. Effect of the pH value of precursor solution on the catalytic performance of V_2O_5 -WO₃/TiO₂ in the low temperature NH₃-SCR of NO_x. *J. Fuel Chem. Technol.* **2014**, *42*, 1455–1463.
- (46) Pearson, R. G. Hard and Soft Acids and Bases. J. Am. Chem. Soc. 1963, 85, 3533–3539.
- (47) Guo, J.; Zheng, Y.; Hu, Z.; Zheng, C.; Mao, J.; Du, K.; Jaroniec, M.; Qiao, S.-Z.; Ling, T. Direct seawater electrolysis by adjusting the local reaction environment of a catalyst. *Nat. Energy* **2023**, *8*, 264–272
- (48) Vojvodic, A.; Nørskov, J. K. Optimizing Perovskites for the Water-Splitting Reaction. *Science* **2011**, 334, 1355–1356.
- (49) Suntivich, J.; May, K. J.; Gasteiger, H. A.; Goodenough, J. B.; Shao-Horn, Y. A Perovskite Oxide Optimized for Oxygen Evolution Catalysis from Molecular Orbital Principles. *Science* **2011**, 334, 1383–1385.
- (50) Wang, Y.-H.; Zheng, S.; Yang, W.-M.; Zhou, R.-Y.; He, Q.-F.; Radjenovic, P.; Dong, J.-C.; Li, S.; Zheng, J.; Yang, Z.-L.; Attard, G.; Pan, F.; Tian, Z.-Q.; Li, J.-F. In situ Raman spectroscopy reveals the structure and dissociation of interfacial water. *Nature* **2021**, *600*, 81–85.
- (51) Shi, H.; Wang, T.; Liu, J.; Chen, W.; Li, S.; Liang, J.; Liu, S.; Liu, X.; Cai, Z.; Wang, C.; Su, D.; Huang, Y.; Elbaz, L.; Li, Q. A sodium-ion-conducted asymmetric electrolyzer to lower the operation voltage for direct seawater electrolysis. *Nat. Commun.* **2023**, *14*, 3934.
- (52) Shen, L. -f.; Lu, B. -a.; Li, Y. -y.; Liu, J.; Huang-fu, Z. -c.; Peng, H.; Ye, J. -y.; Qu, X. -m.; Zhang, J. -m.; Li, G.; Cai, W. -b.; Jiang, Y. -x.; Sun, S. -g. Interfacial Structure of Water as a New Descriptor of the Hydrogen Evolution Reaction. *Angew. Chem., Int. Ed.* **2020**, *59*, 22397–22402.
- (53) Wu, Y.; Wang, L.; Bo, T.; Chai, Z.; Gibson, J. K.; Shi, W. Boosting Hydrogen Evolution in Neutral Medium by Accelerating

- Water Dissociation with Ru Clusters Loaded on Mo₂CT_x MXene. Adv. Funct. Mater. **2023**, 33, 2214375.
- (54) Shang, L.; Zhao, Y.; Kong, X.-Y.; Shi, R.; Waterhouse, G. I. N.; Wen, L.; Zhang, T. Underwater superaerophobic Ni nanoparticle-decorated nickel-molybdenum nitride nanowire arrays for hydrogen evolution in neutral media. *Nano Energy* **2020**, *78*, No. 105375.
- (55) Fan, Y.; Sun, Y.; Zhang, X.; Guo, J. Synergistic effect between sulfur and CoFe alloys embedded in N-doped carbon nanosheets for efficient hydrogen evolution under neutral condition. *Chem. Eng. J.* **2021**, *426*, 131922.
- (56) Kresse, G.; Hafner, J. Ab initio molecular-dynamics simulation of the liquid-metal—amorphous-semiconductor transition in germanium. *Phys. Rev. B* **1994**, *49*, 14251–14269.
- (57) Kresse, G.; Furthmüller, J. Efficient iterative schemes for ab initio total-energy calculations using a plane-wave basis set. *Phys. Rev. B* **1996**, *54*, 11169–11186.
- (58) Perdew, J. P.; Burke, K.; Ernzerhof, M. Generalized gradient approximation made simple. *Phys. Rev. Lett.* **1996**, *77*, 3865–3868.
- (59) Blöchl, P. E. Projector augmented-wave method. *Phys. Rev. B* **1994**, *50*, 17953–17979.
- (60) Henkelman, G.; Uberuaga, B. P.; Jónsson, H. A climbing image nudged elastic band method for finding saddle points and minimum energy paths. *J. Chem. Phys.* **2000**, *113*, 9901–9904.